ELSEVIER

Contents lists available at ScienceDirect

### Materials Science & Engineering A

journal homepage: www.elsevier.com/locate/msea





## Yield stress anomaly and creep of single crystal Ni-base superalloys – Role of particle size

A.B. Parsa<sup>a,\*</sup>, M. Sirrenberg<sup>a</sup>, D. Bürger<sup>a</sup>, M.J. Mills<sup>b</sup>, A. Dlouhy<sup>c</sup>, G. Eggeler<sup>a</sup>

- <sup>a</sup> Institut für Werkstoffe, Ruhr-Universität Bochum, Universitätsstr. 150, 44801, Bochum, Germany
- <sup>b</sup> Materials Science and Engineering Department, The Ohio State University, 2041 College Road, Columbus, OH, 43210-1178, USA
- <sup>c</sup> Institute of Physics of Materials, ACSR, Žižkova 22, 616 62, Brno, Czech Republic

#### ARTICLE INFO

# Keywords: Ni-base superalloy single crystals Constant strain rate Creep 'p-particle size Deformation mechanisms

#### ABSTRACT

In the present work we subject the single crystal Ni-base superalloy ERBO1 (CMSX 4 type) to constant strain rate (CSR) and creep testing at temperatures between 1023 and 1223 K. Three material states are considered which have similar particle volume fractions >60% but differ in  $\gamma'$ -particle sizes (material states S, M and L of particle sizes: 240, 390 and 540 nm). In constant strain rate testing, a yield stress anomaly is observed for all three material states, with a yield stress maximum at 1073 K. This increase of strength with increasing temperature is not observed during creep testing at significantly lower deformation rates in this low temperature high stress creep regime, where different elementary deformation mechanisms govern CSR and creep behavior. In contrast, in the low stress high temperature creep regime, stress/strain rate data pairs from CSR creep tests both show decreasing strength with increasing temperature. It is found that in both types of tests the material state M shows the highest strength (highest yield stress and lowest creep rate). This can be rationalized based on a scenario where both,  $\gamma$ -channel and  $\gamma$ -particle dislocation activities are important. Diffraction contrast transmission electron microscopy is used to study the relevant elementary deformation processes. Details of dislocation arrangements are discussed with a special focus on the role of Kear Wilsdorf (KW) locks,  $\gamma'$ -particle shearing by superlattice stacking faults (extrinsic and intrinsic) and dislocation climb.

#### 1. Introduction

Ni-base single crystal superalloys (SXs) are used to make blades for gas turbines operating in aero engines and power plants [e.g. Refs. [1–6]]. Constant strain rate (CSR) tensile testing [e.g. Refs. [7–11]] and creep testing [e.g. Refs. [12-16]] are two central techniques which are commonly used to measure the response of SXs to monotonic uniaxial tensile loading. In CSR testing, a constant strain rate is imposed, and the resulting stress strain response is recorded. From the resulting stress strain curve, an apparent critical yield stress  $R_{p0.2}$  is retrieved. During tensile creep, a specimen is subjected to a constant stress and the accumulation of strain with time is measured. These tests provide creep curves, the stress and temperature dependencies of creep rates, and rupture times. The <100> direction is the natural solidification direction during Bridgman processing of SX turbine blades [1,5]. Moreover, it is the direction where the elastic modulus has a minimum [17], which helps to minimize thermal stresses during high temperature service. Variations of the order of up to 10° from the targeted <100> growth

direction can occur [5]. Such variation can cause severe deviations in the creep response, as has been recently shown by Heep et al. [18]. In the present work we use a combined Laue/spark erosion technique to obtain precisely oriented CSR tensile and creep specimens (precision: <100>

 $\pm 1^{\circ}$ ) [19].

One objective of the present work is to compare results from CSR and creep testing. Ni-base single crystal superalloys have microstructures, where cuboidal particles ( $\gamma'$ -phase, typical average cube edge length: 400 nm, ordered L1 $_2$  phase) are coherently precipitated in a  $\gamma$ -matrix. Thin  $\gamma$ -channels (fcc crystal structure, typical average channel width: 50 nm) separate the  $\gamma'$ -particles. A second objective of the present work is to investigate, how the size of  $\gamma'$  particles affects CSR and tensile creep results. Transmission electron microscopy (TEM) is used to evaluate the deformation substructures which are associated with CSR and tensile creep testing, and the observed deformation mechanisms are discussed in the light of recent literature.

E-mail address: alireza.basirparsa@ruhr-uni-bochum.de (A.B. Parsa).

 $<sup>^{\</sup>ast}$  Corresponding author.

#### 2. Material and experiments

#### 2.1. Alloy composition and heat treatments

The material investigated in the present work was an alloy of CMSX-4 type, referred to as ERBO/1 [20]. Single crystals were received from Doncasters Precision Casting, Bochum as cast rods (length: 160 mm, diameter: 20 mm). The nominal chemical composition of the alloy is given in Table 1.

The rods were subjected to a solution heat treatment consisting of  $2\,h$  annealing at 1573 K, slow heating (1 K/min) to 1583 K, 6 h annealing at 1583 K followed by air cooling. To establish large (L), medium (M) and small (S)  $\gamma'$ -particle sizes, the solution annealing was followed by a dual step precipitation heat treatment as outlined in Table 2. Temperatures and times of the precipitation heat treatment were chosen based on experimental and calculated volume fraction versus temperature data published for CMSX4 [21–23].  $\gamma'$  volume fractions between 61 and 66% were established.

#### 2.2. Characterization of $\gamma$ ' volume fractions and particle sizes

 $\gamma'$  volume fractions and particle sizes were investigated using a scanning electron microscope (SEM) of type Leo Gemini 1530 VP from Carl Zeiss AG. All SEM investigations were carried out on polished and etched cross sections parallel to {100} planes. Good contrast between the two phases was obtained after etching for 3 s in a solution of 40 ml H<sub>2</sub>O, 20 ml HCl (37%) and 10 ml H<sub>2</sub>O<sub>2</sub>. SEM results obtained for the material states from Table 2 are shown in Fig. 1. Fig. 1a–d and g show micrographs which were taken using secondary electron contrast.  $\gamma'$ -particle sizes and  $\gamma$ -channel widths were measured following a procedure which has been described previously [24,25]. Fast Fourier transformation (FFT) results are presented next to SEM micrographs in Fig. 1b–e and h.

 $\gamma$ -particle sizes  $d_i$  and  $\gamma$ -channel widths  $w_i$  of SX materials, which solidified in [001] direction, are obtained by averaging the dimensions in [100] and [010] directions:

$$d_i = \frac{d_i^{[100]} + d_i^{[010]}}{2} \text{ and } w_i = \frac{w_i^{[100]} + w_i^{[010]}}{2}$$
 (1)

For each material state five micrographs (areas:  $11.4 \times 8.6 \ \mu m^2$ ) were taken from dendritic regions. Between 864 and 4903 particles/channels were evaluated. Histograms of size distributions for the three material states are presented in Fig. 1c–f and i. Average values were obtained as

$$\overline{d}_i = \frac{1}{n} \cdot \sum_{i=1}^n d_i \text{ and } \overline{w}_i = \frac{1}{n} \cdot \sum_{i=1}^n w_i$$
 (2)

To quantify the microstructural scatter, the mean deviations from these mean values  $\Delta \overline{d}$  and  $\Delta \overline{w}$  were determined as

$$\Delta \overline{d} = \frac{1}{n} \cdot \sum_{i=1}^{n} |\overline{d} - d_i| \text{ and } \Delta \overline{w} = \frac{1}{n} \cdot \sum_{i=1}^{n} |\overline{w} - w_i|$$
(3)

Table 3 summarizes the results, listing the number n of particles considered, the mean  $\gamma'$ -sizes  $\overline{d}$  and the mean deviations from these mean values  $\Delta \overline{d}$ , the average  $\gamma$ -channel widths  $\overline{w}$  and their corresponding  $\Delta \overline{w}$  values. Finally,  $\gamma'$  and  $\gamma$  volume fractions  $f_{\gamma'}$  and  $f_{\gamma'}$  were obtained using [26]

Table 2

Three precipitation heat treatments following the post cast solution heat treatment to establish large (L), medium (M) and small (S)  $\gamma'$ -particle sizes. 1st precipitation treatment: 1413 K followed by air cooling. 2nd precipitation treatment: 1143 K followed by air cooling.

Material state	1st precipitation treatment/h	2nd precipitation treatment/h		
L	10	16		
M	4	16		
S	0	16		

$$f_{\gamma} = \frac{\overline{d}^3}{(\overline{w} + \overline{d})^3}$$
 and  $f_{\gamma} = 1 - f_{\gamma}$  (4)

The SEM micrographs in Fig. 1 together with the quantitative metallographic data from Table 3 document that the three material states differ in particle sizes and channel widths while exhibiting similar volume fractions close to 66 % for material states L and M and 61 % for material state S. The scatter in the  $d_i$  and  $w_i$  values naturally affects the precision of the measured volume fractions which, however, show little scatter (<1%) when average results from different micrographs are compared. The FFT results in Fig. 1b, e, and 1h provide insight into differences in the overall particle shapes. For the S condition, there is larger FFT intensity at angles deviating from <010> directions, which indicates that the particles are less cuboidal and start to evolve towards spherical shapes.

#### 2.3. Constant strain rate (CSR) testing

The CSR tests were performed using an electromechanical test rig of type Criterion Model C45.105 from MTS, equipped with a three-zone resistance furnace which allows to reach temperatures up to 1273 K. Precise specimen orientations were established using the iterative Laue/spark erosion procedure documented by Wollgramm et al. [19]. The left side of Fig. 2a shows the geometry of the CSR specimens and schematically illustrates how CSR specimens were mounted in the tensile test rig. The three zones of the furnace were controlled with three NiCr/Ni-thermocouples, which were in direct contact with the specimen and also served as measurement thermocouples.

The temperatures measured with the three thermocouples differed by not more than  $\pm 1$  K. During testing, loads were monitored using a 30 kN load cell. Strains up to 4% (displacements of 0.5 mm) were measured using a high temperature extensometer, where the tips of two ceramic rods were slightly pushed against the specimen (gauge length  $l_0$ : 12 mm). Higher strains were recorded using the cross-head data calculated for a gauge length of 17 mm. The CSR tensile specimens were heated to test temperature under a preload of 150 N. Specimens were kept at this temperature for 20 min prior to testing. CSR tensile tests were performed imposing constant strain rates between  $8.0 \cdot 10^{-5}$  s<sup>-1</sup> and  $1.3 \cdot 10^{-4}$  s<sup>-1</sup>. Most tests were performed using an imposed strain rate of  $3.3 \cdot 10^{-4} \, \text{s}^{-1}$ . Some experiments were interrupted after the yield stress  $R_{p0.2}$  had been reached, to study the elementary processes which govern the yield stress anomaly. Others were deformed to higher strains, to study how well CSR testing captures microstructural softening. Table 4 lists the CSR tests which were performed in the present work.

#### 2.4. Creep testing

Creep tests were performed following the procedure described by Wollgramm et al. [19]. The creep tests are performed under constant

**Table 1**Nominal chemical composition of ERBO/1.

Element/wt%	Al	Co	Cr	Hf	Mo	Re	Ta	Ti	W	Ni
Specification	5.45–5.75	9.3–10.0	6.4–6.6	0.07-0.12	0.5-0.7	2.8-3.1	6.3–6.7	0.9–1.1	6.2-6.6	Bal.

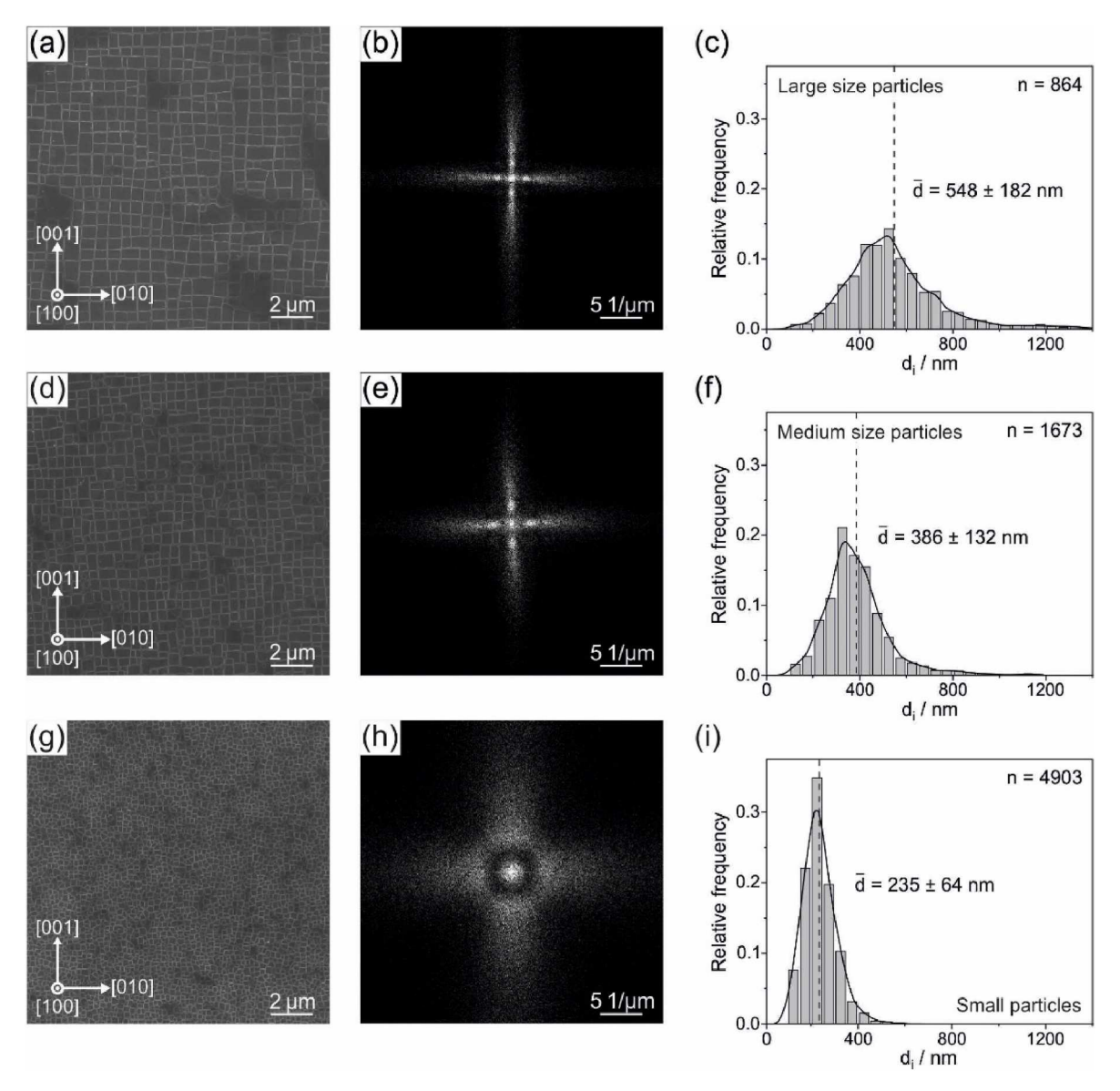


Fig. 1. Micrographs and  $\gamma'$ -particle size distributions for the three heat treatments given in Table 2. (a,b,c) Materials state L. (d,e,f) Material state M. (g,h,i) Material state S. (a,d,g) SEM micrographs. (b,e,h) FFTs (providing insight into average particle shapes). (c,f,i) Histograms with d<sub>i</sub> size distributions.

**Table 3**Quantitative metallographic data retrieved from SEM micrographs using Equations (1)–(4).

Material state	n	$\overline{d}/\mathrm{nm}$	<u>w</u> ∕nm	$f_{\gamma'}/\%$
L	864	$548\pm182$	$81\pm26$	66.1
M	1673	$386\pm132$	$57\pm19$	66.1
S	4903	$235\pm64$	$42\pm14$	61.1

load, where stresses moderately increase according to  $\sigma=\sigma_0\cdot\exp\varepsilon$  [12–16]. The left side of Fig. 2b shows the specimen geometry and illustrates how the specimen was mounted. The specimens were heated up to test temperatures in a furnace with three independently controlled heating zones. The test temperatures were measured at the upper and lower ends of the gauge sections of the specimens with two Pt10Rh/Pt thermocouples (front thermocouple shown in light grey). Two ceramic rod-in-tube extensometers were used to transfer displacements to two linear vertical transducers outside the furnace. The displacement signal for the calculation of true strains was taken as the average of these two measurements. The specimens were heated under a small preload and

the creep test started after the target temperature was reached and thermal equilibrium was established after about 2 h. Conventional creep tests and temperature change experiments were performed as listed in Table 5, where conventional creep tests (performed at a constant load and temperature) are referred to as "monotonic" and temperature change experiments are indicated as "T-change".

#### 2.5. Transmission electron microscopy (TEM)

Material states which were deformed to strains of 2 and 7.5% strain in CSR and 1% strain in creep testing were investigated using a TEM of type FEI Tecnai F20 and a probe corrected JEOL JEM-ARM200F NEO-ARM both operating at 200 kV. The scanning TEM (STEM) diffraction contrast imaging (DCI) was performed using a detector semi angle of 22–114 mrad on a Fischione high angle annular dark field (HAADF) detector. The high-resolution STEM images (HRSTEM) were acquired using an annular dark field (ADF) detector semi angle of 68–280 mrad.

The HRSTEM images were then filtered using Wiener filtering for better contrast. For preparation of TEM samples, a 400  $\mu$ m thick slice was cut from the gauge length of the deformed specimens, which was

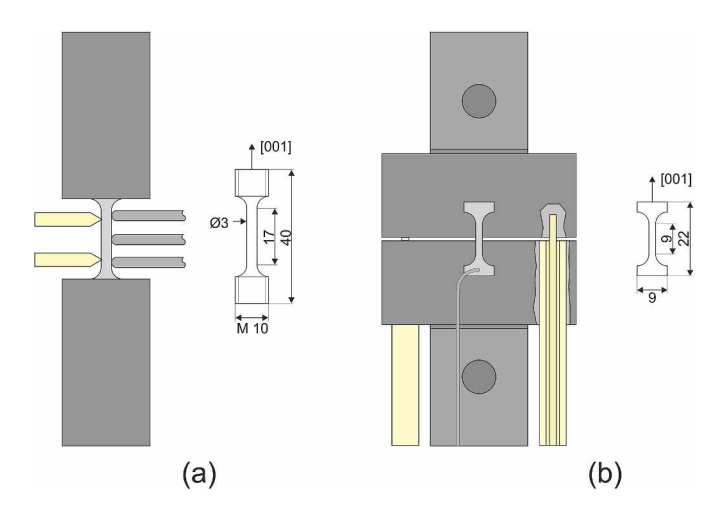


Fig. 2. Schematic illustration of CSR and creep testing. (a) CSR specimen as mounted during testing (left) and specimen geometry/crystallography (right). (b) Flat creep specimen as mounted during testing (left) and specimen geometry/crystallography (right). Thickness of specimen: 2 mm. All values are given in mm.

**Table 4** Overview of all CSR experiments performed in the present work with varying  $\gamma$  particle size and different imposed strain rates.

Material state	Number of tests	Temperature/K	Total strain rate/s <sup>-1</sup>
L	1	1023	$3.3 \cdot 10^{-4}$
L	4	1073	$3.3 \cdot 10^{-4}$
L	1	1123	$3.3 \cdot 10^{-4}$
L	1	1223	$3.3 \cdot 10^{-4}$
M	3	1023	$3.3 \cdot 10^{-4}$
M	5	1073	$3.3 \cdot 10^{-4}$
M	2	1123	$3.3 \cdot 10^{-4}$
M	1	1223	$8.0 \cdot 10^{-5}$
M	2	1223	$3.3 \cdot 10^{-4}$
M	1	1223	$1.3 \cdot 10^{-3}$
S	2	1023	$3.3 \cdot 10^{-4}$
S	3	1073	$3.3 \cdot 10^{-4}$
S	1	1123	$3.3 \cdot 10^{-4}$
S	1	1223	$3.3 \cdot 10^{-4}$

**Table 5**Overview of all creep tests in different stress/temperature regimes and varying material state.

Material state	Type - Number of tests	Stress/MPa	Temperature(s)/ K
L	monotonic - 1	800	1023
L	monotonic - 1	800	1073
L	monotonic - 1	400	1223
L	T-change - 1	700	1043, 1073, 1113
M	monotonic - 1	800	1023
M	monotonic - 2	800	1073
M	monotonic - 5	400, 420, 550, 680	1223
M	T-change - 1	700	1043, 1073, 1113
S	monotonic - 1	800	1023
S	monotonic - 3	800	1073
S	monotonic - 2	400	1223
S	T-change - 1	700	1043, 1073, 1113

then ground to 100  $\mu$ m using emery paper with mesh sizes increasing from #1000 to #2400. Finally, the slices were electrochemically thinned using a TenuPol-5 to obtain electron transparent thin foils. The electrolyte consisted of 75 vol% CH<sub>3</sub>OH, 15 vol% C<sub>3</sub>H<sub>8</sub>O<sub>3</sub> and 10 vol% HClO<sub>4</sub>. Thinning was performed at 267 K using a voltage close to 13 V and a flow rate of 16. Thin foils were taken perpendicular to the direction of the applied stress (foil normal: [001]) and 45° to the direction of

the applied stress (foil normal: [011]). Details regarding the TEM analysis have been described elsewhere [29,29–31,31,32].

#### 3. Results

#### 3.1. Constant strain rate (CSR) testing

Fig. 3 presents CSR tests results from the test temperatures of 1023, 1073 and 1223 K. The three columns in Fig. 3 represent the results obtained for the three particle sizes as indicated. The three rows of Fig. 3 present results which were obtained for the three test temperatures. Engineering yield stresses  $R_{p0.2}$  and elastic moduli E, as determined from the stress strain curves, are given in each figure. Fig. 3a (S/1023 K) shows two curves: one has been interrupted after 2% strain and one was taken through to rupture. Note that the scatter between the two experiments is so small that it is difficult to differentiate between the two curves. Fig. 3b (M/1023 K) shows the results of four experiments, two of which were taken through to rupture. Note that while there is some scatter, the measured engineering yield stresses of the two tests which were deformed beyond the elastic regime are in good agreement. Fig. 3c (L/1023 K) shows one test which was taken through to rupture. For all tests performed at 1023 K, similar values of engineering yield stresses are observed. For all three material states, work hardening after the yield point starts with a smaller increases of stress with strain (first small arrows) followed by a more intense strain hardening (second small arrows) in Fig. 3 a,b and c. The rate of work hardening (slope of stress strain curve) intensifies as the particle size increases from S to L. In Fig. 3d (S/1073 K) two strain stress curves are shown, one interrupted after 2% strain and one of a test which has been taken through to rupture. A sharp maximum in the stress strain curves highlighted by a vertical arrow pointing down suggests that there is a macroscopic yield point, which is followed by a gradual decrease of stress with increasing strain to a local stress minimum, from where the stress increases slightly again. Fig. 3e (M/1073 K) presents three curves which also show this yield point maximum followed by a gradual drop in stress.

For all three material states tested at 1073 K, clear yield points (small downward arrows) are observed. Fig. 3d, e and f. The curves are distinctly different from the curves obtained at 1023 K. The engineering yield stress values differ for the three material states where the maximum is obtained for the material state M and the minimum for material state S. This represents a clear particle size effect on the yield stress anomaly, which is observed at 1073 K, as discussed further below. Fig. 3g, h, and i show the stress strain curves obtained for CSR testing at 1223 K. At this temperature, the engineering yield stress is significantly lower than the values obtained at the lower temperatures. The curves for all material states (S, M and L) show gradual softening after yield, and there is little systematic difference between the three material states.

#### 3.2. Creep testing

Creep experiments which were performed at stresses between 400 and 800 MPa and temperatures of 1023, 1073 and 1223 K are presented in Fig. 4. There only is a small scatter between two experiments performed under the same creep conditions (see two sets of S-data in Fig. 4c and d). In Fig. 4 creep data are presented as conventional strain vs. time plots in Fig. 4a-c and e and as log-linear plots of strain rate vs. strain in Fig. 4b-d and f. Fig. 4a-d shows the creep curve shapes which are characteristic for the low temperature high stress creep regime. Typical features of this creep regime are large on-load strain intervals and two creep rate minima [19,27,28]. Fig. 4e and f shows creep curves which are typically observed in the high temperature and low stress creep regime (e.g. T > 1173 K,  $\sigma <$  500 MPa) [19,29,30]. At 1023 K and 800 MPa, material state S exhibits the highest creep rates and the shortest rupture times. The lowest deformation rates are observed for material state M. Material state L deforms a little faster than material state M. This clearly holds for the deformation rates at the global minima at

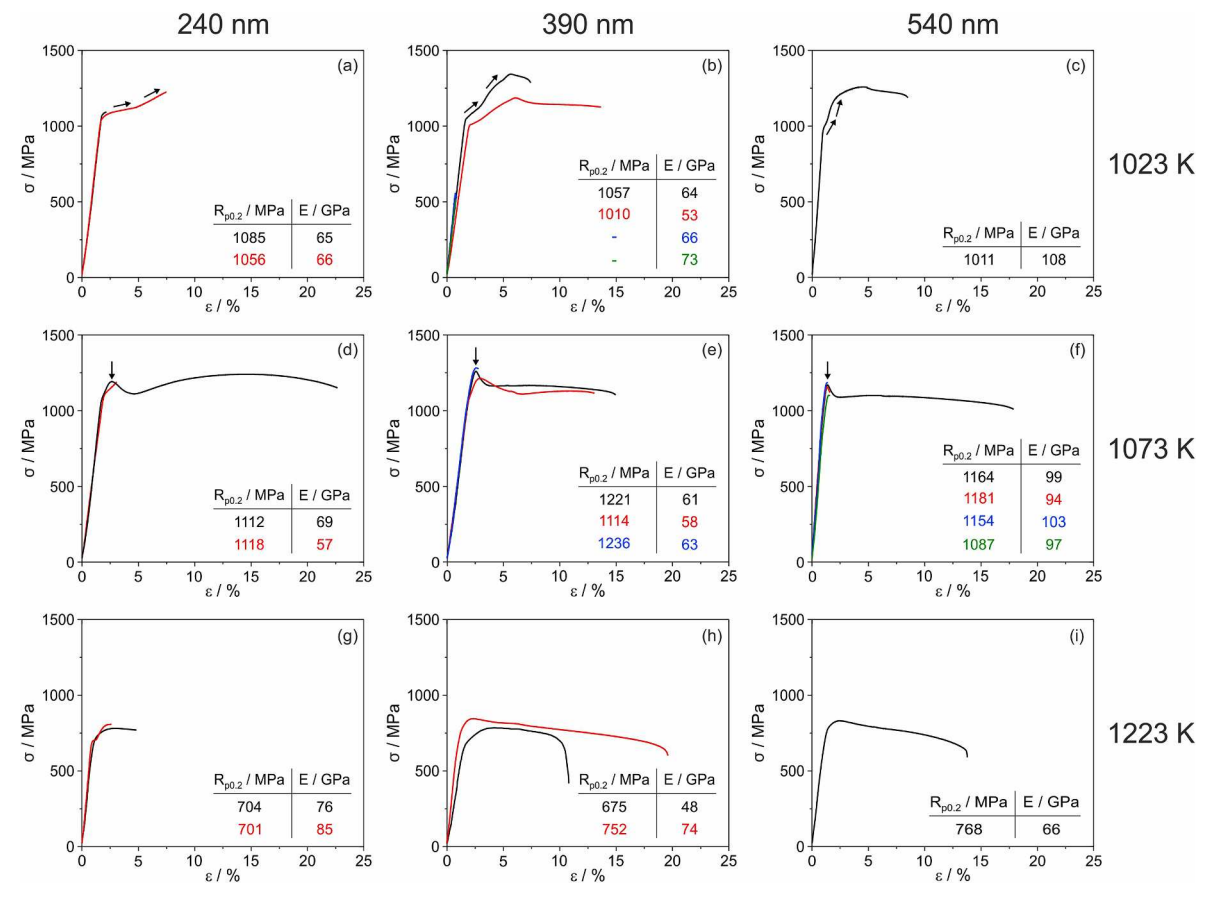


Fig. 3. Stress-strain-curves from CSR tests at: (a,b,c) 1023 K. (d,e,f) 1073 K. (g,h,i) 1223 K. Material state: S (a,d,g), M (b,e,h) and L (c,f,i).

strains between 5 and 6%, Fig. 4b. At 1073 K and 800 MPa, only material state S shows a pronounced and reproducible (two experiments were performed) on-load straining, Fig. 4c and d. The material states M and L no longer exhibit this fast accumulation of strains in the very early stages of creep. The creep rates of all three material states observed at the global minima, which are reached after 2.5% for material states M and L and after 9% for material state S are similar. The 1223 K/400 MPa creep data from the high temperature low stress regime show creep curves with easily distinguishable primary, secondary and tertiary creep regimes. The creep rates observed for the three material states in the early creep stages are similar. In the early stages of creep, no differences between the three material states can be detected. Material state S shows the shortest rupture time, followed by material states L and M:  $t_{\rm R}^{\rm M} > t_{\rm R}^{\rm L} > t_{\rm R}^{\rm S}$ . Minimum creep rates also slightly differ:  $\dot{\epsilon}_{\rm min}^{\rm M} < \dot{\epsilon}_{\rm min}^{\rm L} < \dot{\epsilon}_{\rm min}^{\rm S}$ .

#### 3.3. CSR vs. creep in the low temperature high stress regime

In Fig. 5 we compare the temperature dependence of superalloy strength as observed in CSR for material states S, M, L, and in creep testing for material state M. Fig. 5a shows the temperature dependence of the apparent yield stress,  $R_{p0.2} = f(T)$  observed for an imposed strain rate  $\dot{\epsilon}_{IMPOSED}$  of  $3.3 \cdot 10^{-4}$  s<sup>-1</sup> (test durations: 10–30 min). As outlined in Table 4, some of the tests were repeated between two and five times. For these tests, the results shown in Fig. 5a represent the mean yield stress values together with the mean deviations from these mean values as error bars. Tests which were not repeated appear as single data points.

As was shown in Fig. 3, the deviations in  $R_{p0.2}$  for one test condition were always small. It can be clearly seen that starting at 1023 K the engineering yield stress  $R_{p0.2}$  increases, reaches a local maximum at 1073 K, and then decreases. This represents clear experimental evidence for the presence of a yield stress anomaly (YSA). Below the YSA peak

temperature, the yield stresses obtained for different particle sizes do not differ strongly. However, as mentioned above in relation to Fig. 3a, b, and c, the proportional limit appears to decrease between materials states, S to M to L, while the work hardening rates increase in that order. Consequently, the  $R_{p0.2}$  remains approximately invariant for the three materials states. Likewise, at temperatures well above the YSA peak temperature,  $R_{p0.2}$  values obtained for different particle sizes are similar.

At the temperature of the YSA maximum, there is a clear effect of particle size on the maximum stress. It is found that the material with the medium particle size (material state M) shows the highest peak stress. Increasing the particle size (material state L) results in a decrease of peak stress as compared to the material state M. The material S with the smallest particle size exhibits the lowest strength at the YSA peak temperature. Under CSR testing conditions, the superalloy exhibits a strength maximum at 1073 K. Under creep loading conditions in the YSA temperature range, this is not the case. Fig. 5b shows the temperature dependence of creep rates obtained in a temperature change experiment, described in detail by Bürger et al. [31]. The test was performed at a constant stress of 700 MPa. As shown in Fig. 5b, the temperature change tests started at 1043 K, where the specimen was deformed to 2% so that the secondary creep rate was reached. Then the temperature was increased in two steps, first from 1043 K to 1073 K and then from 1073 K to 1103 K, Fig. 5b. After both temperature changes the creep loading condition was maintained within a strain interval of 1%. As can be seen in Fig. 5b, new secondary creep rates were established after short normal creep rate transients (<0.2%). Here the creep rates increase with increasing temperature. This shows that under creep conditions, at deformation rates between  $10^{-8}$  and  $10^{-6}$  s<sup>-1</sup> (test durations: 10–30 h), the strength of superalloys decreases with increasing temperature.

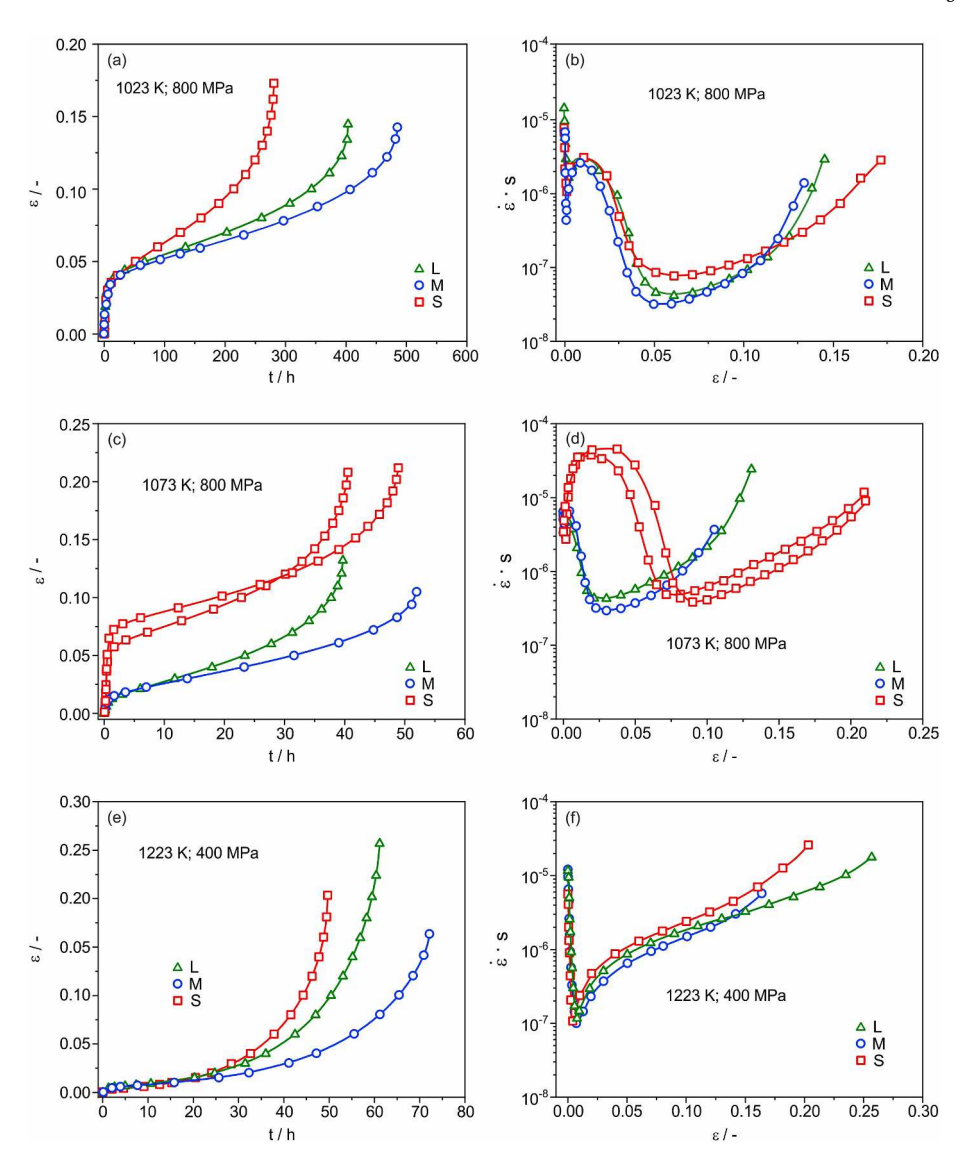
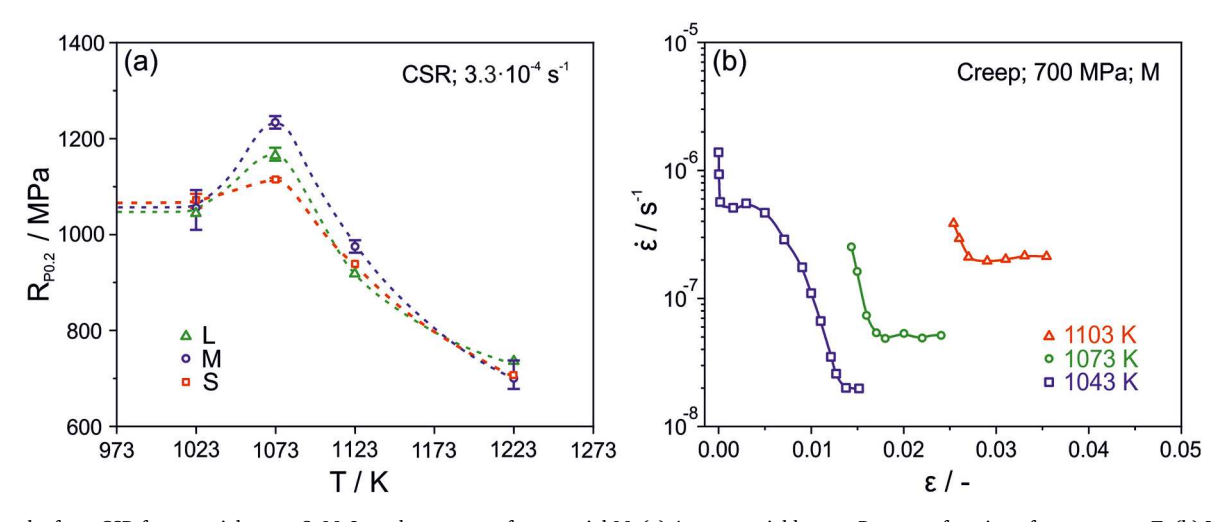


Fig. 4. Creep results of the material states S, M and L in different stress/temperature regimes. Data are shown as strain vs. time (a, c, e) and logarithmic strain rate vs. strain (b, d, f). (a) and (b) 1023 K and 800 MPa. (c) and (d) 1073 K and 800 MPa. (e) and (f) 1223 K and 400 MPa.



**Fig. 5.** Results from CSR for material states S, M, L, and creep tests for material M. (a) Apparent yield stress  $R_{p0.2}$  as a function of temperature T. (b) Logarithmic creep rates plotted as a function of strain measured in a temperature change test with constant temperature creep periods at 1043, 1073 and 1103 K.

#### 3.4. CSR vs. creep results in the high temperature low stress regime

CSR and creep data from the high temperature (1223 K) and low stress regime are presented in Fig. 6. Fig. 6a shows three stress strain curves of CSR experiments performed at imposed strain rates of  $8.0\cdot 10^{-5}$  (interrupted at 4.5%),  $3.3\cdot 10^{-4}$  (taken through to rupture) and  $1.3\cdot 10^{-3}$  s $^{-1}$  (interrupted at 4.5%) In Fig. 6b, creep curves obtained from experiments performed between 420 and 680 MPa are presented as log-linear plots of strain rate vs. strain. The corresponding minimum creep rates are  $1.3\cdot 10^{-7}$ ,  $2.0\cdot 10^{-6}$  and  $2.0\cdot 10^{-5}$  s $^{-1}$ . These results will be discussed later, Fig. 11.

#### 3.5. Microstructure after CSR testing

TEM results from CSR experiments are presented in Fig. 7, with results for the material states with the lowest and highest peak stress at 1073 K (material states S and M). Fig. 7a and b shows microstructures which evolved at 1023 K, below the YSA peak. In Fig. 7a, after 2% strain, there are numerous short dislocation segments present within the  $\gamma'$ precipitates. Some of these have been highlighted by white arrows in a magnified inset in the upper right. Fig. 7b documents the microstructure after failing at about 7.5 % strain. The microstructure contains a higher density of short dislocation segments in the  $\gamma'$ -particles (inset), several dislocation dipoles, and less frequently observed small dislocation loops. Fig. 7c and d document the evolution of the microstructure at 1073 K, where the stress maximum associated with YSA is observed. The two experiments with material states S and M were interrupted at 2%. Additional diffraction contrast imaging using multiple, strong-beam conditions (not shown here for brevity) were used to identify Burgers vectors for these short dislocation segments that are traversing through the thin foil at large angles relative to the [001] foil normal. The results indicate that these short  $\gamma'$  dislocation segments have Burgers' vectors along [101] and [01-1] directions. Tilting experiments showed that they have predominantly screw character. Thus, these are consistent with Kear-Wilsdorf locks (KW locks) [32]. These small segments are also observed in the material state M, Fig. 7d. Fig. 7e shows a weak beam dark field (WBDF) image of such a small segment from material state M. The micrograph was taken using a g/3g contrast condition (g =  $(\overline{2}00)$ ) after tilting the foil about 32° towards the [011] pole, which reveals that the small segment consists of two dislocations, Fig. 7e. When viewed near the [001] zone axis, these short segments would appear as singular lines, Fig. 7f. The projection of a [101] vector for respective tilt angles, under which WBDF images were recorded, is given as white arrows in Fig. 7e and f. The WBDF image in Fig. 7e confirms the presence of KW-locks comprised of two  $\frac{1}{2}$ <101> dislocations that are dissociated largely on a cube plane. Using positive/negative **g**-vector conditions, one can exclude the possibility that these short segments exhibit dipole character. While clear dipole configurations were observed, the most prominent feature within the  $\frac{\gamma}{2}$ -particles are a<101> dislocations in KW lock configurations. Note that these same short, straight segments in identical configurations are observed at 1023 K. Thus, the features highlighted by the white arrows in Fig. 7a and b also represent KW-locks.

At 1073 K, in addition to the presence of KW-locks, stacking faults extend across  $\gamma'$ -particles in material states S and M, Fig. 7c and d. This represents the most obvious distinction between deformation activity at this temperature and at 1023 K. Fig. 8a represents an attempt to quantify the number of KW locks per sample area. After deformation at 1023 K there is an increase by almost a factor of 5 in KW-lock density as strains increase from 2% to 7.5%, a significant change that correlates with the large strain hardening seen at this temperature (Fig. 3a–c).

It is noted that the distribution of defects in the 2%/1023 K microstructure is inhomogeneous with areas in which the  $\gamma'$  particles do not contain any defects, and areas with high defect content such as the region shown in Fig. 7a. For material state S after 7.5 % strain at 1023 K, a more homogeneous distribution of defects throughout the microstructure is observed. Therefore, care has been taken when reporting defect area densities in this inhomogeneous microstructure and averaged values are reported in Fig. 8a. The number density of KW locks after 2% strain shows a slight increase when the test temperature is increased from 1023 to 1073 K. In Fig. 8b, the number ratio of KW locks and stacking faults (SF) to total number of defects (SF + KW) for material states S and M at 1073 K is reported. The share of stacking faults and KW locks are similar for the material state S at peak temperature. But, for material state M, there are more KW locks in the  $\gamma'$ -particles than stacking faults, Fig. 8b. The increase in the KW lock population for material state M is consistent with the higher maximum stress for this microstructure, as shown in Fig. 5a. The presence of KW locks remains important for both microstructures, but stacking fault shearing is also clearly important at the temperature of the YSA maximum and correlates with a dramatic change from hardening (at 1023 K) to softening (at 1073 K). At 1223 K, well beyond the temperature of the YSA, much more dislocation line length is present in the  $\gamma'$ -particles, with dislocations taking on more curved configurations, Fig. 7g and h. Since the foil orientation for these images is [001], curved configurations indicate extensive movement of dislocations on octahedral planes. In addition to dislocation content, the  $\gamma'$ -particles also contain stacking faults.

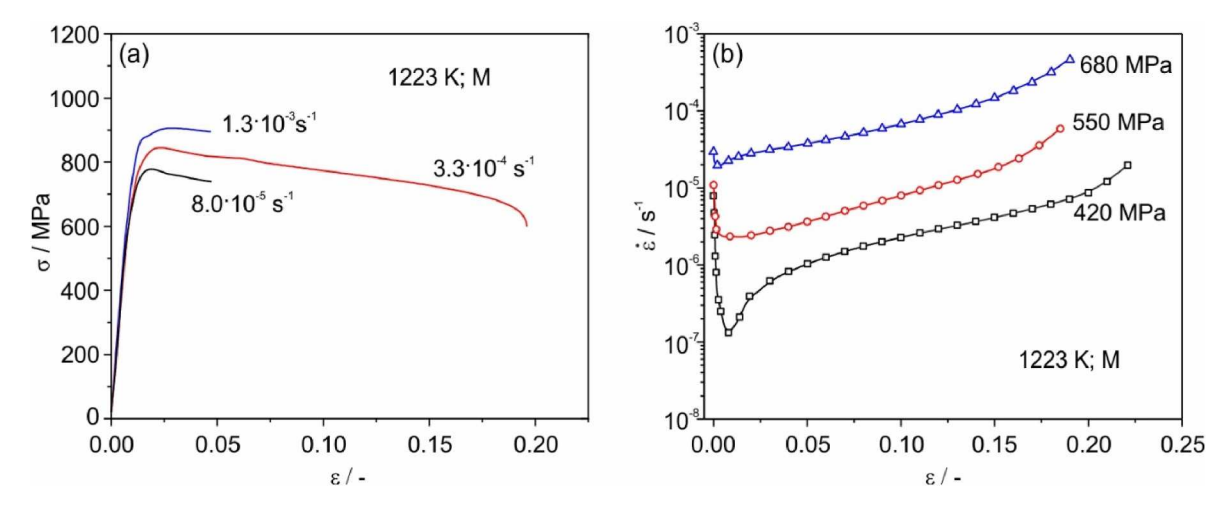


**Fig. 6.** Characteristic stresses and strain rates from creep and CSR experiments at 1223 K imposed/recorded for material state M. (a) Stress strain curves from CSR tests performed at strain rates of  $8.0 \cdot 10^{-5}$ ,  $3.3 \cdot 10^{-4}$  and  $1.3 \cdot 10^{-3}$  s<sup>-1</sup> (Table 4). (b) Plot of strain rates vs. strain from creep tests performed at 420, 550 and 680 MPa (Table 5). This data is represented in a Norton plot below in Fig. 11 and compared with low stress creep data.

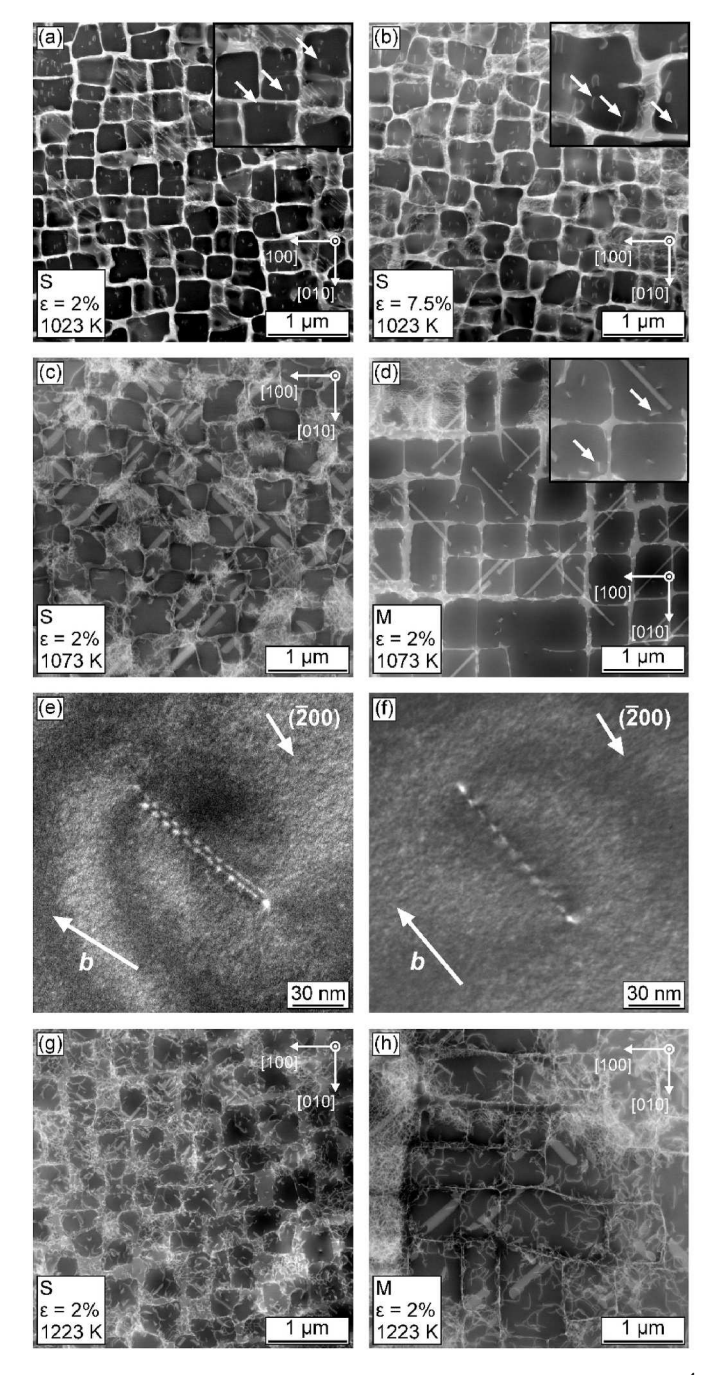


**Fig. 7.** STEM-DCI results obtained after constant strain rate testing at  $3.3 \cdot 10^{-4}$  s<sup>-1</sup>. The test temperature and strain condition for each image is indicated on the figures. (a,b) Material state S at 1023 K after 2 and 7.5% strain). (c,d) Material states S and M at 1073 K after 2% strain. (e,f) KW-lock imaged in weak beam dark field mode, material state M at 1073 K. (g/3g) taken close to [011] and [001] poles, respectively. (foil normal: [001]). (g,f) Material states S and M at 1223 K.

#### 3.6. Microstructure after creep testing

Fig. 9 shows STEM micrographs which were obtained from creep specimens after 1% deformation. The micrograph in Fig. 9a shows the material state S which was interrupted during on-load straining after creep at 1073 K and 800 MPa. A group of well aligned planar faults extend diagonally across the image in orthogonal orientations.

These diagonal configurations indicate that, due to the precise [001] orientation of the samples and the corresponding orientation of the

tensile loading axis, high temperature plasticity proceeds by multiple slip. A distribution of slip events between all four glide planes in the horizontal  $\gamma$ -channels and in the  $\gamma'$ -particles minimizes the global sample rotation in the early stages of creep. In fact, no macroscopic specimen rotation was detected. Fig. 9b shows the material state M deformed at 1073 K and 800 MPa. It contains planar faults which are not aligned as those seen in material state S exposed to the same creep conditions. There appears to be a distinct absence of superdislocations in the  $\gamma'$ -phase at this temperature. In the high temperature low stress creep regime (1223 K, 400 MPa) no planar faults form, Fig. 9c and d. In the case of material state M two  $\gamma$ -particles are highlighted with a white circle, where one can clearly see that two dislocations from the  $\gamma$ -phase jointly shear the  $\gamma$ -phase where they form a superdislocation. Comparing Fig. 9c and d, fewer dislocations and faults in the  $\gamma'$ -phase are observed when particles are smaller. Either cutting is less frequent when particles are smaller or superdislocations are not trapped in the  $\gamma'$  phase because they can reach the other  $\gamma/\gamma'$  interface more rapidly. The presence of extended faulted structures, which is most apparent in Fig. 9a for material state S, could indicate the activity of microtwinning as has been observed in high stress, intermediate temperature creep of superalloys [33–36]. High resolution images using an HAADF detector along a [110] zone axis are shown in Fig. 10. In this condition, two sets of active {111} planes are seen in edge-on configurations, such that twins on these glide planes can be assessed directly. Examination of multiple regions indicate that stacking faults are observed in the  $\gamma'$  precipitates of both intrinsic (Fig. 10b) and extrinsic (Fig. 10c) type. The presence of both fault features suggests the activity of stacking-fault ribbons, as previously reported for [001] tensile conditions by Rae and Reed [27] and others. No multilayer fault structures consistent with microtwinning was observed.

#### 4. Discussion

#### 4.1. Yield stress anomaly (YSA)

In agreement with what has been reported in the literature [5, 37-40], single crystal Ni-base superalloys show a remarkable characteristic: yield stresses increase with increasing temperature, with a yield stress maximum above 1000 MPa at 1073 K. Superalloys inherit this property from their major constituent, the ordered  $\gamma'$ -phase. This behavior of ordered intermetallic phases has been attributed to the cross slip of dislocations from octahedral to cube planes, resulting in the formation of sessile dislocation configurations (KW locks), which rely on thermally activated processes [5,32,41-43]. Indeed, KW locks are observed to be present below and at the YSA peak, Fig. 7 c-e, and Fig. 8b. However, the present work also indicates that stacking fault shearing of  $\gamma'$  commences at 1073 K, the temperature of the YSA maximum stress peak. Stacking faults, on the other hand, are not observed below the peak at 1023 K. These observations therefore indicate that the yield strength anomaly in superalloys may result from an interplay between APB-coupled dislocation glide and stacking fault shearing. The former involves the configuration of identical ½<101> channel dislocations, enabling them to cooperatively enter the  $\gamma'$  particles. Glide of a<101> APB coupled dislocations on {111} planes can occur athermally, while KW lock formation by cross-glide onto {001} planes requires thermal activation. The formation of stacking faults within the  $\gamma'$  particles is attributed to the configuration of dissimilar ½<101> channel dislocations, forming a leading 1/3<112> partial dislocation, which then can enter the particle, leaving behind an SISF. Previous detailed analysis of the 1/3<112> leading partials in crept material structures [44-47] indicate that its glide requires significant thermal activation due to local atomic reordering to eliminate wrong nearest-neighbor bonds, and segregation of Co and Cr which is commonly reported after deformation at intermediate temperature.

A hypothesis to explain the yield strength anomaly in this superalloy is the following: Below the YSA peak, APB shearing of coupled  $\frac{1}{2}$ <101> dislocations occurs, as indicated by the presence of KW locks. Note that

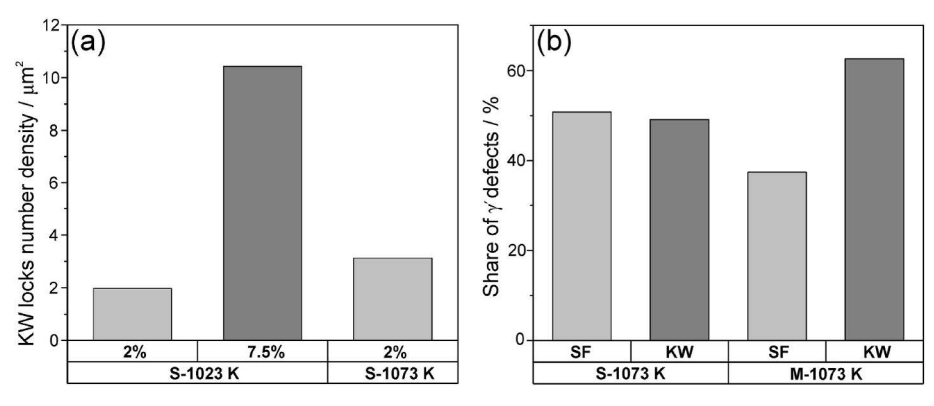


Fig. 8. (a) Number of Kear Wilsdorf locks per area in the material state S after CSR testing at 1023 and 1073 K. (b) Share of superlattice stacking faults and Kear Wilsdorf locks. Here the number ratio of SF and KW faults to total number of defects in the  $\gamma'$ -particles is reported for materials state S and M at 1073 K.

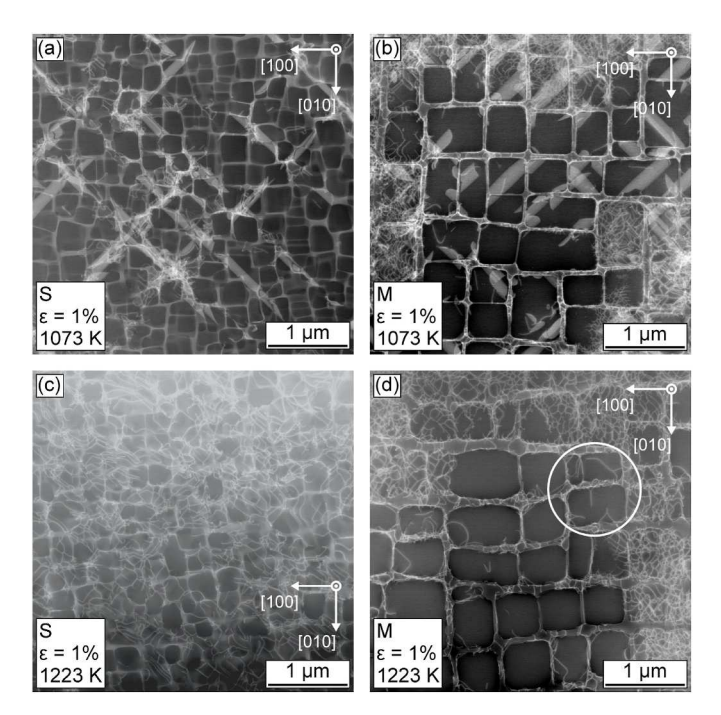


Fig. 9. STEM-DCI micrographs taken after 1% plastic strain of creep testing. (a) and (b): 1073~K, (c) and (d) 1223~K. (a) and (c) Material state S (small particles). (b) and (d) Material state M (medium particle size).

at this temperature, strong work hardening is also observed, and TEM analysis indicates that the density of KW locks increases with increasing strain, Fig. 8a. At the peak temperature, KW locks continue to form, potentially more frequently leading to the increased yield strength. However, at this temperature, there is sufficiently rapid diffusion to enable climb and re-configuration of dissimilar ½<110> dislocations, as well as reordering and Co/Cr segregation, such that 1/3<112> partials can successfully enter and shear the  $\gamma'$  particles. This hypothesis is further supported by the fact that no stacking faults were observed at 1023 K, even in the specimen deformed to 7.5%. As stacking fault shearing becomes possible, ½<101> channel dislocations are consumed by this more rate-dependent process, and fewer channel dislocations are available to undergo APB coupled shearing. It is also noted that instead of strong work hardening as seen below the peak at 1023 K, a yield point followed by flow softening is found consistently on the flow curves for CSR tests at 1073 K, Fig. 3 d to f. The presence of gradual softening after a yield plateau has been also reported by Wang-Koh and coworkers [48] in single crystal CMSX-4 deformed in tension at 1023 K. The yield plateau is attributed by these authors to the initial activation of APB

coupled shearing at small strain by the operation of a single ½<110> slip system. In their study, a single slip system is initially activated since the tensile axis of single crystals is approximately 5° away from precise [001] alignment. The yield plateau persists for several percent plastic strain, and then gives way to a softening response, which is attributed to the onset of stacking-fault shearing based on direct TEM investigation of samples interrupted at various strain levels through this transition. These authors [48] also suppose that stacking fault shearing is more strongly time-dependent and diffusion-mediated than is APB-coupled shearing of similar ½<101> dislocations. Following similar reasoning, the distinctive, sharp yield point (YSA stress maximum) observed in the present work is attributed to the fact that the single crystal samples are precisely aligned along [001] such that multiple slip systems of  $\frac{1}{2}$ <101> dislocations are activated in the y channels from the onset of plastic deformation. Consequently, the reaction of dissimilar ½<101> dislocations can occur immediately at small plastic strains, near the yield point, and enable diffusion-mediated stacking fault shearing to commence. A summary of the observed mechanisms operative in the  $\gamma$ particles below and at the YSA peak is given in Table 6. This Table also includes observed mechanisms at higher temperature for CSR and under selected creep conditions.

#### 4.2. CSR vs. creep in different stress/temperature regimes

In the previous section we discussed dislocation mechanisms which rationalize YSA of Ni-base superalloys at temperatures below 1073 K. In this temperature regime (1023 K < T < 1073 K), the yield stress increases with increasing temperature, Fig. 5a. In contrast, in this same temperature regime, the creep response exhibits no anomaly in strength, as shown in Fig. 5b. As summarized in Table 6, under creep conditions, stacking fault shearing is observed predominantly at 1073 K, while no KW locks are found. This evidence further supports the connection between KW lock formation and the YSA observed under CSR conditions. Thus, under the lower strain rate conditions in the creep tests, the diffusion-mediated stacking fault shearing process appears to dominate, with some evidence for superdislocation shearing also observed (for material state M). At higher temperature (1273 K), stacking faults are no longer observed and diffusion-controlled climb processes play a central role, with superdislocation shearing of  $\gamma$ ' dominating. These mechanisms have been described extensively in the literature [29–49].

An even broader view of the high temperature plasticity (creep and CSR) response over 8 orders of magnitude in strain rate is shown in Fig. 11 at 1223 K, which includes minimum creep rate data in the low stress range previously published for the same alloy [50]. The predominant shearing process observed in the  $\gamma'$  particles at these conditions are also indicated in Fig. 11. Several features are notable. (1) The strain rate/stress data pairs from CSR tests and creep tests can be represented by a continuous curve, suggesting that there is some continuity

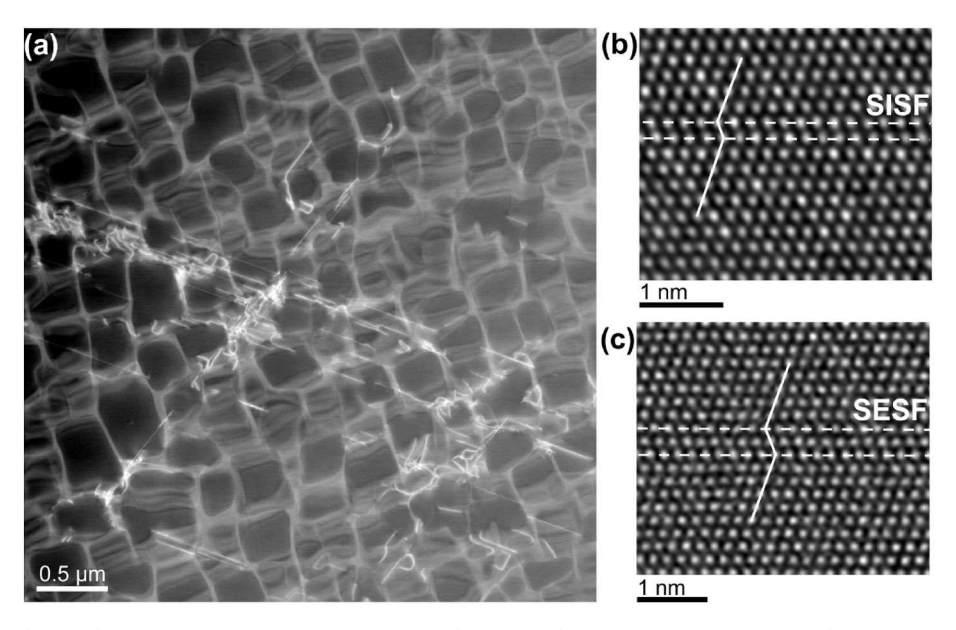


Fig. 10. Stacking faults in deformed microstructure after creep at 1073 K and 800 MPa (lower mag overview micrograph in Fig. 9a, particle size: S, foil normal [011]). (a) ADF-STEM image shows the stacking faults along two (111) planes. Filtered HRSTEM images in (b) and (c) document presence of both superlattice intrinsic (SISF) and extrinsic (SESF) stacking faults, respectively.

Table 6 Compilation of the observed deformation mechanisms pertinent to  $\gamma'$  phase in the present study. KW: Kear-Wilsdorf locks. SF: stacking fault shearing. SD: Superdislocation  $\gamma'$  particle shearing. The predominant mechanism for a given condition is boldfaced. These assessments are based on samples arrested at small strain levels (approx. 2%).

$\gamma'$ particle size	CSR		Creep	
	S	M	S	M
Low Temp. (1023 K)	KW	-	-	-
Peak Temp. (1073 K)	KW + SF	KW + SF	SF	SF + SD
High Temp. (1223 K)	SF + SD	SF + SD	-	SD

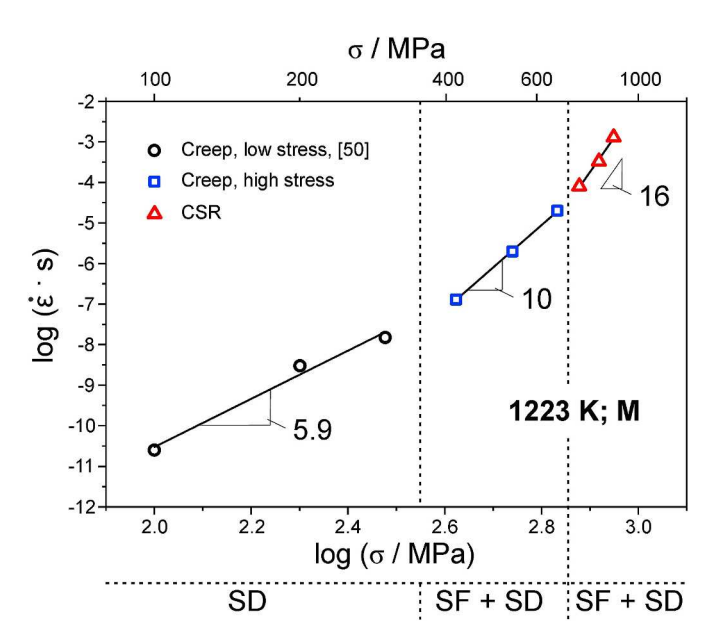


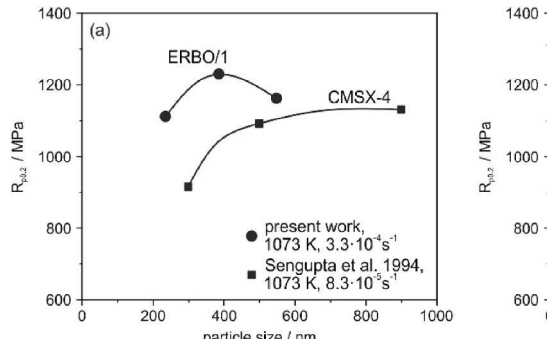
Fig. 11. A Norton plot showing stress/strain-rate data from low and high stress creep and CSR tests at 1223 K. Results from current study are shown, along with data from a previous work [50]. The predominant mechanisms in the  $\gamma^\prime$  particles are also indicated, SD is for superdislocation shearing and SF is for stacking fault shearing.

of mechanisms regardless of the deformation mode, and that CSR and creep tests for similar conditions can be expected to yield similar mechanical behavior. The stress exponent n is a useful technological parameter to describe stress dependencies of secondary creep rates in a limited stress range [19,51,52]. (2) Indeed, the same two  $\gamma'$  shearing processes associated with stacking faults and superdislocations are operative over this broad range of conditions from 400 to 900 MPa (3) Nevertheless, extrapolating from CSR to creep conditions using a simple Norton plot will likely lead to systematic overprediction of creep strength. (4) There is a distinct decrease in the stress exponent with decreasing stress/strain rate, with a value of about 6 for the lowest stresses/strain rates. (5) The change in stress exponent at the lowest stress range correlates with a transition from SD + SF dominating at higher strain rate to superdislocations dominating  $\gamma'$  shearing at low strain rates.

Thus, there appears to be a linkage between transitions in CSR/creep behavior and transitions in the  $\gamma'$  shearing processes. These correlations which required extensive TEM level investigation, can help guide further modeling of the overall creep response. It should be noted that  $\gamma'$ shearing processes must be closely linked with deformation processes that are occurring in the  $\gamma$  channels. This point has been made numerous times [e.g. 5,28,29,31, 51, 54-58], and is additionally supported in the present work. That  $\gamma'$  shearing is not the only rate limiting process in creep/CSR conditions is further emphasized by the fact that the shearing by superdislocations or stacking faults are both supposed to be diffusion controlled, and thus only weakly dependent on stress [30,54–58]. That the actual stress exponents are large, and increase with stress/strain rate, indicates that further model development is needed to include climb and plasticity events in the  $\gamma$  channels, coupled with  $\gamma$ ' shearing mechanisms, in order to develop a comprehensive deformation model for a broad range of conditions.

#### 4.3. Effect of particle size on yield stress maxima in CSR tests

There is general agreement on the fact that the size of  $\gamma'$ -particles affects high temperature strength. However, in the case of single crystal superalloys, different results have been reported, Fig. 12. Our results on ERBO/1 clearly show that at a constant volume fraction, an intermediate particle size (material state M) results in the highest maximum yield stress. It is difficult to comment on the results of other authors, where



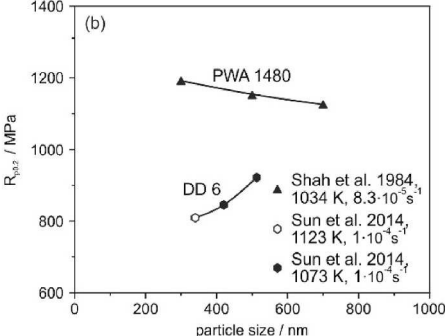


Fig. 12. Dependence of the apparent yield stress peak measured in high temperature CSR tests on particle size. (a) Results from the present work ( $f_{\gamma}$ : 66%) and from Sengupta et al. [38] ( $f_{\gamma}$ : 70%). (b) Results reported by Shah et al. [37] ( $f_{\gamma}$ : not reported) and Sun et al. [39] ( $f_{\gamma}$ : 68 and 70%).

information on precise specimen orientations and particle volume fractions is missing or incomplete [37–39]. As one would expect, results differ in different temperature/stress regimes and for different alloys. While our results presented in Fig. 12a clearly show that there is a YSA stress maximum for the medium particle size, other researchers have not observed a maximum and report decreasing or increasing [38,39] yield strength values with increasing particle size, Fig. 12a and b.

With the aid of Fig. 13 the particle size dependence of the yield stress peak at 1073 K is now discussed. At a constant volume fraction of 66%, the dependence of the average channel width w on average particle size d is given by:

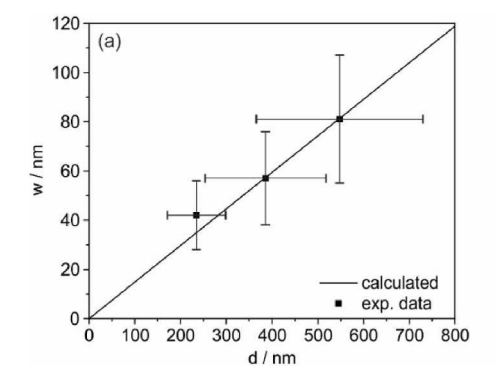
$$w = \sqrt[3]{d^3/0.66} - d \tag{5}$$

Fig. 13a shows this dependence together with the experimental values (mean values and scatter bands) which were determined in the present work. It is clear that  $\gamma$ -channels widen when  $\gamma'$ -particle sizes increase at constant volume fraction. Particle strengthening of alloys with coherent ordered particles has received considerable attention in the literature, where mostly small and widely spaced particles were considered in between which dislocations bow out [59,60]. SXs have high-volume fraction of particles where dislocations squeeze into narrow  $\gamma$ -channels. The accumulation of plastic strain relies on two coupled processes: Dislocation plasticity in the γ-channels and cutting of  $\gamma'$ -particles. It seems reasonable to assume that dislocation plasticity in the  $\gamma$ -channels is promoted when  $\gamma$ -channels widen, i.e. when particle sizes increase at a constant volume fraction, Fig. 13a. By this reasoning, for material state L, there should be the greatest opportunity for matrix dislocations to enter and configure themselves at the  $\gamma/\gamma'$  interface, and then shear the  $\gamma'$ , either by coupled APB shearing or stacking fault formation. Thus, in materials state L, the necessary precursor to shearing

(channel activity) is easiest relative to the other two material states.

Conversely, material state S has narrow channels; however, it can be argued that dislocations which are still present at the interface can enter and shear the smaller  $\gamma'$  particles more easily since the is particles are more rounded than those in states M and L, which are more cuboidal in shape. The importance of  $\gamma'$  particle curvature in determining the ease of dislocation entry has been quantitatively explored by Zhou et al. [58] using phase filed calculations. They find that particles with small radius of curvature (i.e. the curved interfaces of state S, as evidenced in the FFTs of Fig. 1) should be more easily sheared due to local line tension effects. Finally, by these arguments, material state M is strongest because it has the optimum combination of  $\gamma$ -size (particles are not small enough to be easily cut) and  $\gamma$ -channel width (channel dislocation activity not too strongly promoted). An additional trend noted earlier is that the rate of work hardening at 1023 K (below the YSA peak) depends on material state, with the rate of hardening increasing from S to M to L, as shown in Fig. 3a-c. The dramatic hardening at this temperature is attributed KW lock formation. These results imply that the rate of KW lock formation could be dependent upon the size of the  $\gamma'$  particles, with more frequent locking occurring in larger particles. This hypothesis seems reasonable considering that the probability of initiating a cross-slip event from {111} to {001}, and beginning the KW lock formation process, should scale with the length of the APB-coupled dislocation aligned along screw orientation in the  $\gamma'$  particle.

Two microstructural findings require further discussion. At 1223 K the material state S shows very few planar faults following CSR testing (this result is not shown for brevity). We suggest that in this case, diffusion-controlled climb of dislocations out of  $\gamma$ -channels is dominant and  $\gamma'$ -phase cutting is not required for dynamic recovery. In a first order approximation we can estimate the diffusion distance x associated with the test time t, which in our case is 60 s (test is interrupted after 2% at an



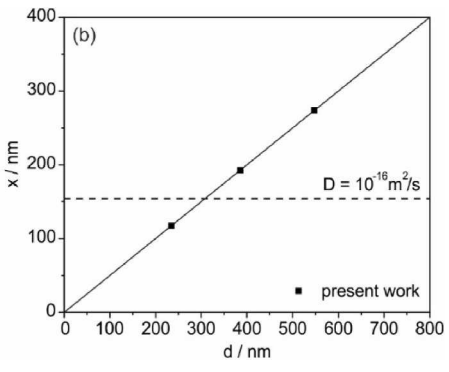


Fig. 13. Schematic illustrations for discussing Particle size dependency of the YSA maximum observed for ERBO/1 in Fig. 12a. (a) At a constant volume fraction of 61% (material state S) and 66% (material states M and L), channel widths w increase with increasing particle size d. (b) Climb distance x required to bypass particles without cutting. Available time of high temperature exposure allows for overclimbing of small particles in material state S, the particles of material states M and L are too large and must be cut.

imposed strain rate of  $3.3 \cdot 10^{-4} \text{ s}^{-1}$ ):

$$x = 2 \cdot \sqrt{D \cdot t} \tag{6}$$

In Equation (6), D represents an appropriate diffusion coefficient. Using a value of  $10^{-16}$  m²/s (close to the value reported for the diffusion of Re in pure Ni between 1173 and 1273 K [5]), we obtain a diffusion distance of 159 nm. This value is shown as a horizontal line in Fig. 13b. The maximum required climb distance plotted on the y-axis, is given by half of the particle size, which is the maximum climb distance which a dislocation has to overcome by climb in order to get out of a central  $\gamma$ -channel region between two  $\gamma'$ -particles. This estimate is in line with a scenario where 60 s are sufficient for diffusion-controlled climb of dislocations around particles in material state S. In material states M and L, the diffusion distances cannot be overcome in this short time period, and thus the more efficient shearing processes (in terms of diffusion-mediated events [58]) associated with pair-wise cutting of superdislocations is active instead.

#### 4.4. Effect of particle size on minimum creep rates during creep testing

Results on the dependence of minimum creep rates on particle sizes are presented in Fig. 14. The results of the present work are shown in Fig. 14a. There is a clear creep rate minimum for the material state M at creep temperatures of 1023 and 1073 K, full and half empty diamonds in Fig. 14a. This minimum is no longer clearly detectable at 1223 K (empty diamonds in Fig. 14a). At this temperature diffusion is faster. The creep tests take significantly longer than the CSR tests mentioned above, and dislocations have enough time to overcome the distances required for the diffusion-controlled climb. Therefore, recovery processes associated with shearing of  $\gamma'$  particles are not predominantly activated, as evidenced by the STEM micrographs in Fig. 9c and d. This would explain why at this temperature the influence of  $\gamma'$  particle size on the minimum creep rate is minimal. Even though at 1073 K the deformation

mechanisms which govern the material response to CSR and creep loading differ (YSA vs. regular temperature dependence), particle sizes show comparable effects. The material state M shows the highest mechanical resistance, in both, CSR testing (highest yield stress, Fig. 11a) as well as in creep testing (lowest minimum creep rate, Fig. 4). Two groups reported creep rate minima for intermediate particle sizes previously [61,62] (Neumeier et al. [61] for volume fractions of 70%; Nathal et al. [62] without mentioning volume fractions), Fig. 14b and c. Other researchers, who have not documented their particle volume fractions, report increasing [63] and decreasing [64,65] tendencies, Fig. 14c and d. The best creep resistance of the material state M is again, like in CSR testing, a consequence of the interaction of dislocation processes in the  $\gamma$ -channels and the cutting of  $\gamma$ -particles. In case of material state S, particle cutting by planar faults is essentially absent after CSR (1223 K, maximum yield stress: 700 MPa) and creep testing (1223 K, 400 MPa), Figs. 7f and 10c. For material state M, cutting of  $\gamma'$ -particles is observed at 1223 K. However, it occurs by planar fault cutting in CSR-testing, while it proceeds by pairwise cutting of two individual dislocations which move by a combined process of glide and climb, which has been described in the literature for the high temperature low stress creep regime [29,30,54–56]. Four of these cutting events are highlighted by a white circle in Fig. 9d.

#### 4.5. Onload straining

Onload straining, as shown in Fig. 4, has been observed previously and has been discussed in the literature [27,53,66–71]. This effect is intriguing, because the material reacts with a significant accumulation of strain (e.g. 5%) in short time intervals (long enough to be recorded, e.g. 1 h) before normal secondary and tertiary creep set in and rupture occurs after much longer times (order of magnitude, i.e. 100 h). It was reported that onload straining reacts to the particle size and the precise orientation of specimens [27,53,66–71]. Rae et al. [27,66] have suggested that onload straining is a high stress effect, which ceases when

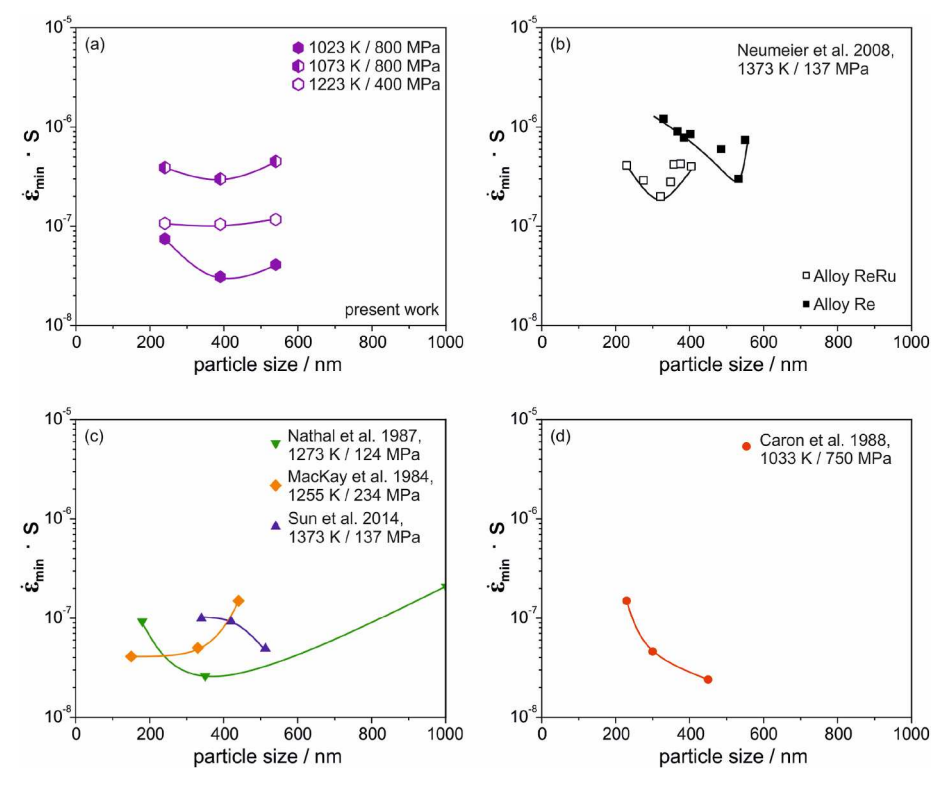


Fig. 14. Dependence of minimum creep rate on particle size reported by different authors. (a) Results from present work ( $f_{\gamma}$ : 66%). (b) Results from Neumeier et al. [61] ( $f_{\gamma}$ : 71% [Re] and 73% [ReRu]). (c) Results from Nathal et al. [62] ( $f_{\gamma}$ : not reported), MacKay et al. [63] ( $f_{\gamma}$ : not reported), Sun et al. [64] ( $f_{\gamma}$ : not reported). (d) Caron et al. [65] ( $f_{\gamma}$ : not reported).

lower stresses are applied. In the present work, at 1023 K and 800 MPa, all three material states show onload straining. In contrast, after a temperature increase of 50 K, only material state S exhibits onload straining, Fig. 4c and d. It is interesting to compare the TEM micrographs shown in Fig. 9a (material state S, onload straining) and b (material state M, no onload straining), which both show planar faults in the  $\gamma$ -phase. Fig. 9a (material state S) clearly shows that individual planar faults form macroscopic bands. The planar faults in Fig. 9b (material state M) can also be part of more than one particle, however no macroscopic bands are observed. In our case (precisely oriented specimens), multiple slip events govern deformation which does not lead to lattice rotations as suggest by MacKay and Maier [68], Fig. 9a. The fact that onload straining ceases for material states M and L, when increasing the temperature from 1023 to 1073 K at a constant stress, is in line with a view that an increase of temperature promotes a more homogeneous deformation. Our CSR results show no sign of a sudden macroscopic strain burst. This suggests that onload creep straining also requires time.

#### 5. Summary and conclusions

In the present work, the Ni-base single crystal superalloy ERBO/1 (CMSX-4 type) was subjected to high temperature constant strain rate (CSR) and constant load creep testing. Microstructures were analyzed comprehensively using scanning electron microscopy for  $\gamma'$  volume fractions, particle sizes and shapes, channel widths, and using scanning transmission electron microscopy for analysis of dislocation and planar fault structures. Experiments were performed at temperatures between 1023 and 1223 K. We use different heat treatments to establish three material states, which exhibit similar  $\gamma'$ -volume fractions above 60% and differ in the size of the cuboidal coherent  $\gamma'$ -particles. The three material states exhibit average cube edge lengths of 235 (material state S), 386 (material state M) and 549 nm (material state L). From the results obtained in the present study the following conclusions can be drawn.

- (1) In CSR testing (imposed deformation rate:  $3.3 \cdot 10^{-4} \text{ s}^{-1}$ ) ERBO1 shows a yield stress anomaly (YSA), with a sharp stress maximum at 1073 K (yield point behavior). While the strength observed in CSR testing increases up to this temperature, this does not hold for constant stress creep testing. When increasing the temperature from 1043 to 1103 K, secondary creep rates increase from  $2 \cdot 10^{-8}$  to  $3 \cdot 10^{-7}$  s<sup>-1</sup>. The difference in typical strain rates used in CSR and creep testing is clearly of critical importance.
- (2) Direct TEM investigation confirms that different deformation mechanisms operate in the two testing modes in the regime of the YSA. In CSR testing, APB shearing of  $\gamma'$  by superdislocations and formation of KW locks, dominate below the YSA maximum, while diffusion-mediated stacking fault shearing of  $\gamma'$  commences at the temperature of the YSA maximum. It is postulated that a higher frequency of KW lock formation may indeed lead to the YSA, but that the maximum and subsequent softening at higher temperature is due to the onset of time- and temperature-dependent stacking fault shearing. In contrast, under creep conditions, shearing by stacking faults is observed at similar temperatures without any evidence for KW lock formation or superdislocations within the  $\gamma'$  particles.
- (3) At higher temperature (1223 K), above the YSA regime, the strain rate/stress data pairs from CSR and creep tests can be rationalized by a continuous curve on a Norton plot over 8 orders of magnitude is strain rate. Direct TEM investigation indicates a transition in  $\gamma'$  shearing processes from superdislocation dominated behavior at low strain rates, to a combination of superdislocation and stacking fault shearing at higher strain rates (after both creep and CSR testing).
- (4) The material state M shows the highest strengths, featuring the highest yield stress maximum (CSR testing) and the lowest secondary creep rates (creep testing). It is hypothesized that material

state S is softer because small particles can be easily cut or by-passed by climb (particles are not cut when deformed at 1223 K). Prior to planar fault cutting, dislocations need to enter  $\gamma$ -channels. This is easier for material state L than for material state M. The material state M is strongest, because its particles are large enough to make cutting difficult while channels are not yet sufficiently wide for easy channel entering of dislocations. This qualitative explanation of dependence of high temperature strength on average particle size also holds for creep loading conditions.

(5) In the low temperature high stress creep regime, onload straining is observed during creep testing, where in the very early stages of creep, strains of the order of 5% accumulate in a short time interval (order of magnitude: 1 h). Subsequently, creep seems to proceed by normal secondary and tertiary creep (order of magnitude of duration of creep test: 100 h). For material state S, TEM micrographs show evidence for the activation of all four glide systems with corresponding Schmid factors of 0.41. At 1023 K and 700 MPa, all three material states show onload straining. In contrast, at 1073 K and 700 MPa, onload straining is only observed for material state S. Further work is required to fully explain the phenomenon of onload straining.

#### CRediT authorship contribution statement

A.B. Parsa: Writing – review & editing, Writing – original draft, Visualization, Validation, Software, Methodology, Investigation, Formal analysis. M. Sirrenberg: Writing – review & editing, Visualization, Software, Investigation, Formal analysis, Data curation. D. Bürger: Writing – review & editing, Validation, Software, Investigation, Data curation. M.J. Mills: Writing – review & editing, Writing – original draft, Validation, Supervision, Methodology, Investigation. A. Dlouhy: Writing – review & editing, Software, Methodology. G. Eggeler: Writing – review & editing, Writing – original draft, Supervision, Resources, Project administration, Methodology, Funding acquisition, Conceptualization.

#### Declaration of competing interest

The authors declare that they have no known competing financial interests or personal relationships that could have appeared to influence the work reported in this paper.

#### Data availability

Data will be made available on request.

#### Acknowledgment

The authors AP, MS, DB and GE acknowledge funding through projects A1 and A2 of the collaborative research center SFB/TR 103 by the Deutsche Forschungsgemeinschaft (DFG). MJM acknowledges NSF DMREF Program under grant #1922239 and the Alexander von Humboldt program. AD acknowledges support from CSF under contract 20-11321S.

#### References

- M. McLean, Directionally Solidified Materials for High Temperature Service, The Metals Society, London, 1983.
- [2] J. Lacaze, A. Hazotte, Directionally Solidified Materials Nickel-Base Superalloys for Gas-Turbines, 1990.
- [3] M. Durand-Charre, The Microstructure of Superalloys, CRC Press, Boca Raton, 1997
- [4] M.J. Donachie, S.J. Donachie, Superalloys: A Technical Guide, second ed., ASM International, Materials Park, Ohio, 2002.
- [5] R.C. Reed, The Superalloys: Fundamentals and Applications, Cambridge University Press, Cambridge, 2006.

- [6] T.M. Pollock, S. Tin, Nickel-based superalloys for advanced turbine engines: chemistry, microstructure, and properties, J. Propul. Power 22 (2) (2006) 361–374
- [7] R.R. Jensen, J.K. Tien, Temperature and strain rate dependence of stress-strain behavior in a nickel-base superalloy, Metall. Trans. A 16 (1985) 1049–1068.
- [8] W.W. Milligan, S.D. Antolovich, Yielding and deformation behavior of the single crystal superalloy PWA 1480, Metall. Trans. A 18A (1987) 85–95.
- [9] D. Mukherji, H. Gabrisch, W. Chen, H.J. Fecht, R.P. Wahi, Mechanical behaviour and microstructural evolution in the single crystal superalloy SC16, Acta Mater. 45 (1997) 3143–3154.
- [10] X. Zhang, T. Jin, N.R. Zhao, Z.H. Wang, X.F. Sun, H.R. Guan, Z.Q. Hu, Effect of strain rate on the tensile behavior of a single crystal nickel-base superalloy, Mater. Sci. Eng., A 492 (2008) 364–369.
- [11] K. Hrurkay, D. Kaoumi, Tensile deformation behavior of a nickel based superalloys at different temperatures, Mater. Sci. Eng., A 599 (2014) 196–203.
- [12] F. Garofalo, Fundamentals of Creep and Creep-Rupture in Metals, The Macmillan Company, London, 1965.
- [13] R.W. Evans, B. Wilshire, Creep of Metals and Alloys, Institute of Materials, London, 1985.
- [14] J.P. Poirier, Creep of crystals: high-temperature deformation processes in metals. Ceramics and Minerals, Cambridge University Press, New York, 1985.
- [15] J. Cadek, Creep in Metallic Materials, Elsevier, Amsterdam, 1988.
- [16] M. Kassner, Fundamentals of Creep in Metals and Alloys, third ed., Butterworth-Heinemann, Oxford, 2015.
- [17] K. Demtröder, G. Eggeler, J. Schreuer, Influence of microstructure on macroscopic elastic properties and thermal expansion of nickel-base superalloys ERBO/1 and LEK94, Mater. Sci. Eng. Tech 46 (2015) 563–576.
- [18] L. Heep, D. Bürger, C. Bonnekoh, P. Wollgramm, A. Dlouhy, G. Eggeler, The effect of deviations from precise [001] tensile direction on creep of Ni-base single crystal superalloys, Scripta Mater. 207 (2022) 114274.
- [19] P. Wollgramm, D. Bürger, A.B. Parsa, K. Neuking, G. Eggeler, The effect of stress, temperature and loading direction on the creep behavior of Ni-base single crystal superalloy miniature specimens, Mater. High Temp. 33 (2016) 346–360.
- [20] A.B. Parsa, P. Wollgramm, H. Buck, C. Somsen, A. Kostka, I. Povstugar, P.P. Choi, D. Raabe, A. Dlouhy, J. Mueller, E. Spiecker, K. Demtröder, J. Schreuer, K. Neuking, G. Eggeler, Advanced scale bridging microstructure analysis of single crystal Ni-base superalloys, Adv. Eng. Mater. 17 (2015) 216–230.
- [21] K. Serin, On the influence of stress state, stress level and temperature on gammachannel widening in the single crystal superalloy CMSX-4, Mater. Sci. Eng., A 387–389 (2004) 133–137.
- [22] V. Yardley, I. Povstugar, P.P. Choi, D. Raabe, A.B. Parsa, A. Kostka, C. Somsen, A. Dlouhy, K. Neuking, E.P. George, G. Eggeler, On local phase equilibria and the appearance of nanoparticles in the microstructure of single-crystal Ni-base superalloys, Adv. Eng. Mater. 18 (2016) 1556–1567.
- [23] O.M. Horst, D. Schmitz, J. Schreuer, P. Git, H. Wang, C. Körner, Thermoelastic properties and γ'-solvus temperatures of single-crystal Ni-base superalloys, J. Mater. Sci. 56 (2021) 7637–7658.
- [24] L. Cao, P. Wollgramm, D. Bürger, A. Kostka, G. Cailletaud, G. Eggeler, How evolving multiaxial stress states affect the kinetics of rafting during creep of single crystal Ni-base superalloys, Acta Mater. 158 (2018) 381–392.
- [25] O.M. Horst, D. Adler, P. Git, H. Wang, J. Streitberger, M. Holtkamp, N. Jöns, R. F. Singer, C. Körner, G. Eggeler, Exploring the fundamentals of Ni-based superalloy single crystal (SX) alloy design: chemical composition vs. microstructure, Mater. Des. 195 (2020) 108976.
- [26] R. Bürgel, Handbuch Hochtemperatur-Werkstofftechnik, Vieweg Verlag, Wiesbaden, 2006.
- [27] C.M.F. Rae, R.C. Reed, Primary creep in single crystal superalloys: origins, mechanisms and effects, Acta Mater. 55 (2007) 1067–1081.
- [28] X. Wu, P. Wollgramm, C. Somsen, A. Dlouhy, A. Kostka, G. Eggeler, Double minimum creep of single crystal Ni-base superalloys, Acta Mater. 112 (2016) 242–260.
- [29] L. Agudo Jacomé, P. Nörtershauser, J.K. Heyer, A. Lahni, J. Frenzel, A. Dlouhy, C. Somsen, G. Eggeler, High-temperature and low-stress creep anisotropy of singlecrystal superalloys, Acta Mater. 61 (2013) 2926–2943.
- [30] L. Agudo Jacomé, P. Nörtershauser, C. Somsen, A. Dlouhy, G. Eggeler, On the nature of γ' phase cutting and its effect on high temperature and low stress creep anisotropy of Ni-base single crystal superalloys, Acta Mater. 69 (2014) 246–264.
- [31] D. Bürger, A. Dlouhý, K. Yoshimi, G. Eggeler, On the stress and temperature dependence of low temperature and high stress shear creep in Ni-base single crystal superalloys, Mater. Sci. Eng., A 795 (2020) 139961.
- [32] B.H. Kear, H.G.F. Wilsdorf, Dislocation configurations in plastically deformed polycrystalline Cu<sub>3</sub>Au alloys, Trans. Metall. Soc. AIME 224 (1962) 382–386.
- [33] M.G. Ardakani, M. McLean, B.A. Shollock, Twin formation during creep in single crystals of Ni-based superalloys, Acta Metall. 47 (1999) 2493–2602.
- [34] G.B. Viswanathan, S. Karthikeyan, P.M. Sarosi, R.R. Unocic, M.J. Mills, Microtwinning during intermediate temperature creep of polycrystalline Ni-based superalloys: mechanisms and modelling, Philos. Mag. A 86 (2006) 4823–4840.
- [35] L. Kovarik, R. Unocic, J. Li, P. Sarosi, C. Shen, Y. Wang, M.J. Mills, Microtwinning and other shearing mechanisms at intermediate temperatures in Ni-base superalloys, Prog. Mater. Sci. 54 (2009) 839–873.
- [36] D. Barba, E. Alabort, S. Pedrazzini, D.M. Collins, A.J. Wilkinson, P.A.J. Bagot, M. P. Moody, C. Atkinson, A. Jerusalem, R.C. Reed, On the microtwinning mechanism in a single crystal superalloy, Acta Mater. 135 (2017) 314–329.
- [37] D.M. Shah, D.N. Duhl, The Effect of Orientation, Temperature and gamma prime size on the yield strength of a single crystal nickel base superalloy, in: M. Gell, et al. (Eds.), Proceedings of Superalloys, TMS, Warrendale, 1984, pp. 105–114.

- [38] A. Sengupta, S.K. Putatunda, L. Bartosiewicz, J. Hangas, P.J. Nailos, M. Peputapeck, F.E. Alberts, Tensile behavior of a new single-crystal nickel-based superalloy (CMSX-4) at room and elevated temperatures, J. Mater. Eng. Perform. 3 (1994) 73–81.
- [39] N.R. Sun, L.T. Zhang, Z.G. Li, A.D. Shan, Effect of heat-treatment on microstructure and high-temperature deformation behavior of a low rhenium-containing single crystal nickel-based superalloy, Mater. Sci. Eng. A-Struct. 606 (2014) 417–425.
- [40] E. Nembach, The high temperature peak of the yield strength of γ'-strengthened superalloys, Mater. Sci. Eng., A 429 (1–2) (2006) 277–286.
- [41] P.B. Hirsch, Y.Q. Sun, Observations of dislocations relevant to the anomalous yield stress in L1<sub>2</sub> alloys, Mater. Sci. Eng., A 164 (1–2) (1993) 395–400.
- [42] D.C. Chrzan, M.J. Mills, Criticality in the plastic deformation of L1<sub>2</sub> intermetallic compounds, Phys. Rev. B Condens. 50 (1994) 30–42.
- [43] P. Veyssiere, Yield stress anomalies in ordered alloys: a review of microstructural findings and related hypotheses, Mater. Sci. Eng., A 309 (2001) 44–48.
- [44] V.A. Vorontsov, L. Kovarik, M.J. Mills, C.M.D. Rae, High resolution electron microscopy of dislocation ribbons in CMASX-4 superalloy single crystals, Acta Mater. 60 (2012) 4866–4878.
- [45] Y. Rao, T.M. Smith, M.J. Mills, M. Ghazisaeidi, Segregation of alloy elements to planar faults in γ'-Ni3Al, Acta Mater. 148 (2018) 173–184.
- [46] X. Wu, A. Dlouhy, Y.M. Eggeler, E. Spiecker, A. Kostka, C. Somsen, G. Eggeler, On the nucleation of planar faults during low temperature and high stress creep of single crystal Ni-base superalloys, Acta Mater. 144 (2018) 642–655.
- [47] D. Bürger, A. Dlouhý, K. Yoshimi, G. Eggeler, How nanoscale dislocation reactions govern low-temperature and high-stress creep of Ni-base single crystal superalloys, Crystals 10 (2020) 134.
- [48] Y.M. Wang-Koh, O.M.D.M. Messe, C.W.M. Schwalbe, C.N. Jones, C.M.F. Rae, The effect of strain rate on the tensile deformation behavior of single crystal, Ni-based superalloys, Metall. Mater. Trans. A 45A (2023) 1456–1468.
- [49] P. Wollgramm, H. Buck, K. Neuking, A.B. Parsa, S. Schuwalow, J. Rogal, R. Drautz, G. Eggeler, On the role of Re in the stress and temperature dependence of creep of Ni-base single Crystal superalloys, Mater. Sci. Eng., A 628 (2015) 382–395.
- [50] A.B. Parsa, D. Bürger, T.M. Pollock, G. Eggeler, Misfit and the mechanism of high temperature and low stress creep of Ni-base single crystal superalloys, Acta Mater. 265 (2024) 119576.
- [51] A.M. Brown, M.F. Ashby, On the power-law creep equation, Scripta Metall. Mater. 14 (1980) 1297–1302.
- [52] C. Schuh, D.C. Dunand, An overview of power-law creep in polycrystalline β-titanium, Scripta Mater. 45 (2001) 1415–1421.
- 53] T. Link, M. Feller-Kniepmeier, Shear mechanisms of the γ'-phase in single-crystals and their relation to creep, Metall. Trans. A 23 (1992) 99–105.
- [54] G. Eggeler, A. Dlouhy, On the formation of (010)-dislocations in the γ'-phase of superalloy single crystals during high temperature low stress creep, Acta Mater. 45 (1997) 4251–5262.
- [55] R. Srinivasan, G.F. Eggeler, M.J. Mills, γ'-cutting as rate-controlling recovery process during high-temperature and low-stress creep of superalloy single crystals, Acta Mater. 48 (2000) 4868–4878.
- [56] P.M. Sarosi, R. Srinivasan, G. Eggeler, M.V. Nathal, M.J. Mills, Observations of a<010> dislocations during the high-temperature creep of Ni-based superalloy single crystals deformed along the [001] orientation, Acta Mater. 55 (2007) 2509–2518.
- [57] H. Long, Y. Liu, D. Kong, H. Wei, Y. Chen, S. Mao, Shearing mechanisms of stacking fault and anti-phase-boundary forming dislocation pairs in the γ' phase in Ni-based single crystal superalloy, J. Alloy. Compnd. 724 (2017) 287–295.
- [58] N. Zhou, C. Shen, M.J. Mills, J. Li, Y. Wang, Modeling displacive-diffusional coupled dislocation shearing of γ' precipitates in Ni-base superalloys, Acta Mater. 59 (2011) 3484–3497.
- [59] B. Reppich, Particle strengthening, in: H. Mughrabi (Ed.), Materials Science and Technology, Vol. 6 (Plastic Deformation and Fracture of Materials), VCH Wiley, Weinheim, 1993.
- [60] E. Nembach, Particle Strengthening of Metals and Alloys, John Wiley and Sons, New York, 1997.
- [61] S. Neumeier, F. Pyczak, M. Göken, The influence of Ruthenium and Rhenium on the local properties of the γ-and γ'-phase in Nickel-base superalloys and their consequences for alloy behavior, in: R.C. Reed, et al. (Eds.), Proceedings of Superalloys 2008, TMS, Warrendale, 2008, pp. 109–119.
- [62] M.V. Nathal, Effect of initial gamma prime size on the elevated-temperature creepproperties of single-crystal nickel-base superalloys, Metall. Trans. A 18 (1987) 1961–1970.
- [63] R.A. MacKay, L.J. Ebert, Factors which influence directional coarsening of γ' during creep in nickel-base superalloy single crystals, in: M. Gell, et al. (Eds.), Proceedings of Superalloys, TMS, Warrendale, 1984, pp. 135–144.
- [64] N.R. Sun, L.T. Zhang, Z.G. Li, A.D. Shan, The effect of microstructure on the creep behavior of a low rhenium-containing single crystal nickel-based superalloy, Mater. Sci. Eng., A 606 (2014) 175–186.
- [65] P. Caron, Y. Ohta, Y. Nakagawa, T. Khan, Creep deformation anisotropy in single crystal superalloys, in: D.N. Duhl (Ed.), Proceedings of Superalloys, TMS, Warrendale, 1988, pp. 215–224.
- [66] C.M.F. Rae, N. Matan, D.C. Cox, M.A. Rist, R.C. Reed, On the primary creep of CMSX-4 superalloy single crystals, Metall. Mater. Trans. A 31 (2000) 2219–2228.
- [67] G.R. Leverant, B.H. Kear, The mechanism of creep in gamma prime precipitationhardened nickel-base alloys at intermediate temperatures, Metall. Trans. A 1 (1970) 491–498.
- [68] R.A. MacKay, R.D. Maier, The influence of orientation on the stress rupture properties of nickel-base super-alloy single-crystals, Metall. Trans. A 13 (1982) 1747–1754.

- [69] A.A. Hopgood, J.W. Martin, The creep behaviour of a nickel-based single-crystal superalloy, Mater. Sci. Eng., A 82 (1986) 27–36.
  [70] M. Feller-Kniepmeier, T. Kuttner, [011] creep in a single-crystal nickel-base superalloy at 1033 K, acta metall, Materials 42 (1994) 3167–3174.
- [71] H. Murakami, T. Yamagata, H. Harada, M. Yamazaki, The influence of Co on creep deformation anisotropy in Ni-base single crystal superalloys at intermediate temperatures, Mater. Sci. Eng., A 223 (1997) 54–58.